Steel and Composite Structures, Vol. 9, No. 4 (2009) 349-366
DOI: http://dx.doi.org/10.12989/scs.2009.9.4.349

Loading capacity of simply supported composite slim beam with deep deck

Yongjiu Shi, Lu Yang*, Yuanqing Wang and Qiuzhe Li

Department of Civil Engineering, the Key Laboratory of Structural Engineering and Vibration of China Education Ministry, Tsinghua University, Beijing 100084, China
(Received November 6, 2007, Accepted May 4, 2009)

Abstract. The composite slim beam has become popular throughout Europe in recent years and has also been used on some projects in China. With its steel section encased in a concrete slab, the steel-concrete composite slim beam can provide the floor construction with minimum depth and high fire resistance. However, the design method of the T-shape steel-concrete composite beam is no longer applicable to the composite slim beam with deep deck for its special construction, of which the present design models are not available but mainly depend on experiences. The elevation of the flexural stiffness and bending capacity of composite slim beams with deep deck is rather complicated, because the influences of many factors should be taken into account, such as the variable section dimensions, development of cracks and non-linear characteristics of concrete, etc. In this paper, experimental investigations have been conducted into the flexural behavior of two specimens of simply supported composite slim beam with deep deck. The emphases were laid on the bonding force on the interface between steel beam and concrete, the stress distribution of beam section, the flexural stiffness and bending capacity of the composite beams. Based on the experimental results, the reduction factor of equivalent stress distribution in concrete flange is suggested, and the calculation method of flexural stiffness and bending capacity of simply supported slim beams are proposed.

Keywords. simply supported composite slim beam; experimental study; bending resistance; flexural stiffness; deep deck.

1. Introducton

The composite slim beam originated in Scandinavia was called “Thorbeam”, which consisted of two channel sections welded to a flat plate and it became popular there. This new type of composite beam has many advantages, such as low structural height, fast construction, efficient fire resistance and good serviceability (Chen, *et al*. 2002). So far, some different types of composite slim beam have shown up, but the structural behavior of such composite beams is not well understood.

The Helsinki University of Technology has conducted tests on nine simply supported slim beams, and parametric studies were made of the flexural behavior of the beams. The tests indicated that interface slippage in composite slim beams with reinforcing bars was very small and could be neglected (Lu, *et al.* 1995). Whereafter, the Helsinki University of Technology made a study of the behavior of beam-column connections in a building frame consisting of slim beams. Two tests with bare steel connections and four tests with composite connections were also conducted (Mikko 2000). Experiments on eight

* Corresponding Author, Email: lyang00@mails.tsinghua.edu.cn

slim beams possessing the same section dimensions but different ratios of reinforcement and different load conditions were carried out in Trento University (Bernuzzi, *et al.* 1995). From the experiments, beams were all full shear connected and the ratio of reinforcement had a significant influence on the loading capacity of connections. Whereafter, a study was carried out to deal with different aspects of performance and design of slim floor beams, and a graphical method of which the semi-continuity was considered was proposed for the sequential phases of construction and service (Zandonini, *et al.* 2003). As an alternative to the slim floor, the "slimdek", which comprises a rolled asymmetric steel section and a deep composite slab offers further economy and improved composite action (Lawson, *et al.* 1998), as shown in Fig. 1. Three beam tests were carried out on the asymmetric slim floor beam and the tests demonstrated that considerable composite action can be achieved. Then, the design methods of steel beam in construction stage and composite slim beam in composite stage were proposed (Lawson, *et al.* 1998, 1999). According to these methods, the equivalent stress distribution is adopted but the reduction factor of peak stress is suggested to be 0.45 without experimental verification. In the stiffness calculation, the composite section is supposed to be consistent with the Bernoulli's principle without verification and the cracking of concrete is not taken into account which brings on unsafe results. A two 6 m × 6 m bay slim floor was conducted in City University, London to investigate the combined action of the beam and slab, the effect of cracking and openings in beams and slab and loading bearing capacities of the floor under different load distributions (Lawson, *et al.* 1999). Three tests were conducted on the behavior of the edge beams in Darmstadt University of Technology composite slim floor, and the results showed that the edge beams were governed by torsion (Lange 2006). FE models of different element types were established to simulate the loading behaviour of simply supported composite slim floors and determine the effective width in the slab (Yang, *et al.* 2006 and Queiroz and De Paula 2000). The results promise an advantageous possibility to increase the assumed ratios of the effective width in serviceability.

The Steel Construction Institute (SCI) has recently completed a design guide for composite beams using precast concrete of hollow core or solid plank section (Hicks and Lawson 2003), and from the tests on three full-scale composite beams, it has been demonstrated that the composite slim beams with hollow core units may be designed using the current standards (Eurocode 4) for composite construction with slight modifications (Hicks, *et al.* 2006). However, the design guide is for T-shape composite beams and that of the composite slim beams is still limited especially for composite slim beams with deep deck.

In recent years, an increasing application of the composite floor with slim beam in shallow floor systems has shown up and many researches are made on fire resistance of the composite slim beams (Sha 2001, Bailey 1999, Makelainen and Ma 2000, Lu and Zhang 2005), composite slim frames (Ma and Makelainen 2006) and composite slim slabs (Sha 2001, Borgogno and Fontana 1998, 2000 and Bailey

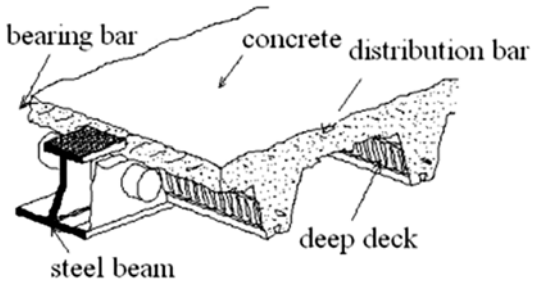

Fig. 1 Composite slim beam with deep deck

2003) in many countries.

In this paper, the design and test results of two specimens of frame composite slim beam with deep deck under monotonic loading have been introduced. The bonding force on the interface between steel beam and concrete, the stress distribution of beam section, the flexural stiffness and bending capacity of the composite beams have been studied. Based on the test results, the reduction factor of equivalent stress distribution in concrete flange is suggested, and the formulas of flexural stiffness and bending capacity are proposed.

2. Experimental investigation

2.1 Geometric dimensions and constructional details of specimens

Two specimens, SLB1 and SLB2, have been fabricated in the same geometric dimensions (Fig. 2). In SLB2, the bottom part of interface between steel beam and concrete below the top plate of deep deck were separated by plastic membrane, as illustrated in Fig. 2. The geometric dimensions are as follows: beam span is 6 m, width of concrete slab is 0.75 m and the longitudinal reinforcement is Φ12@150.

The transverse rebar were folded to constraint the concrete around the top flange of the steel beam and enhance the bonding force between them. Since there are not deep decks for slim beam in China currently, in these tests, MMR-238 corrugated metal profile has been used, the height of which is 180 mm, as shown in Fig. 3.

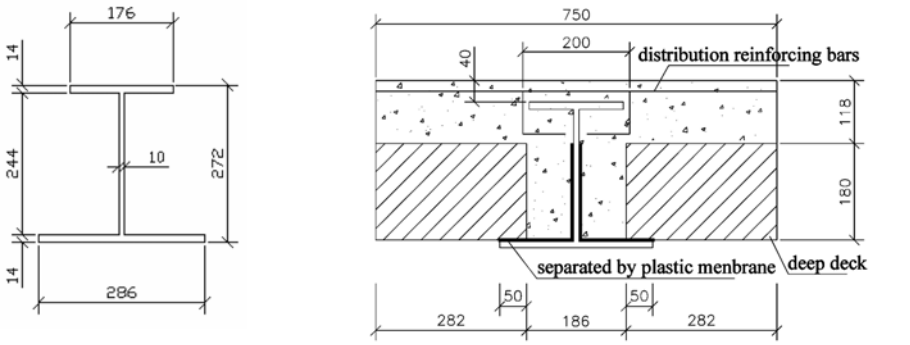

(a) Steel section (b) Composite section (separation on the interface of SLB2)

Fig. 2 Section dimensions

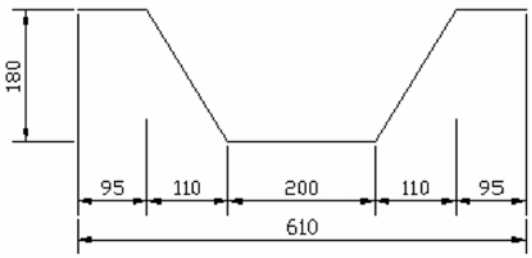

Fig. 3 MMR-238 corrugated metal profile

The strength grades of steel used in the test is Q235 and lightweight aggregate concrete CL25 is adopted. The two specimens were fabricated simultaneously, and the mechanical properties of the concrete and steel are illustrated in Tables 1 and 2 respectively.

2.2 Loading and measurement

The test scene is shown in Fig. 4. As shown in Fig. 5, three loading jacks are used to simulate the uniformly distributed load and the loading cell 1-8 is laid under the jack to record the load. Five displacement meters 1-1, 1-2, 1-3, 1-4, and 1-5 are laid on the bottom flange of steel beam to record the deflection during the tests. In addition, two extensometers 1-6 and 1-7 are laid on either beam end respectively to measure the slippage on the interface.

The strain gauges 3-1~3-7, 2-1~2-7 are applied on the steel beam and the surface of the concrete in the composite section at the midspan respectively, as illustrated in Fig. 6.

Table 1 Material properties of concrete

Axial compressive strength $f_{c,k}$ (N/mm^2)	Young's modules E (10^3 N/mm^2)	Density (kg/m^3)
31.56	17.93	1559.68

Table 2 Mechanical properties of Q235-B steel and rebars

Yield strength f_y (N/mm^2)	Young's modulus E (10^3 N/mm^2)	Yield strain ($\mu\varepsilon$)	Ultimate strength f_u (N/mm^2)
311.20	203.47	1534.57	495.33

Fig. 4 Test scene

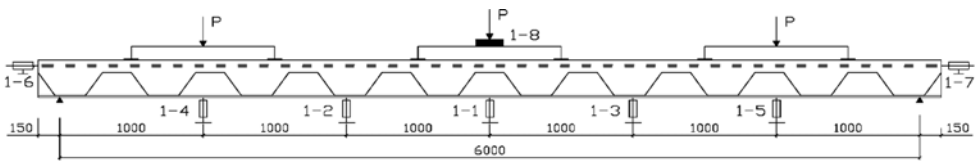

Fig. 5 Test set-up

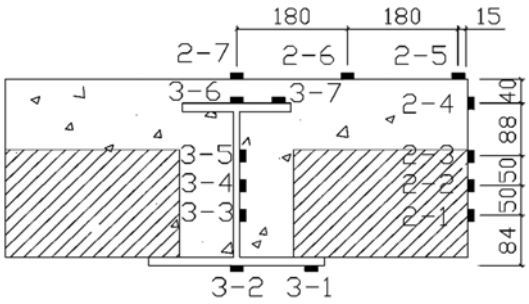

Fig. 6 Distribution of strain gauges

2.3 Test results

2.3.1 Experimental phenomena

The two specimens performed similar loading behavior. In the initial loading phase, both of them were at linear elastic stage. Then the first crack originated at the midspan and it extended perpendicularly to the sloped side of the deep deck. As the applied load of SLB1 reached 72.5% (69.0% for SLB2) of the ultimate value, the bottom flange of midspan steel beam began to yield, the concrete cracks widened and the trend of the load-deflection curve indicated the beginning of the elastic-plastic phase.

When the applied load reached 97% (for both two specimens) of the ultimate value, the top flange of the steel beam began to yield and the main crack widened fast. Both the specimens had a similar failure mode, and FSB1 could be taken for example to illustrate the failure mode of the composite frame beam, as shown in Fig. 7. In the whole loading process, the maximum slip at the beam end was less than 0.2 mm.

2.3.2 Moment-deflection curves at midspan

The specimens were loaded by displacement with a step of 5mm. Before the displacement of the specimen at midspan reached 1/20 of the length of the beam (30 mm), the two composite beams behaved with linear elasticity, with the elastic limit 289.9 kN·m(SLB1) and 297.2 kN·m(SLB2) respectively. Nonlinear behavior could be observed after the applied load beyond the elastic limit and the deformation of both specimens showed good ductility. The ultimate capacity of SLB1 is

SLB1 SLB2

Fig. 7 Failure modes

399.4 kN·m with the displacement of 105 mm at the midspan, while the ultimate capacity of SLB2 is 430.4 kN·m with the displacement of 120 mm at the midspan. The moment-deflection curves of both specimens at midspan are illustrated in Fig. 8.

From Fig. 8, the moment-deflection curves of the two specimens show less difference, especially in the elastic phase, which indicates that the separation on the interface in SLB2 imposes little influence on the loading capacity of the composite beam.

2.3.3 Transverse distribution of strain in the composite section

As shown in Fig. 5, three strain gauges: 2-5, 2-6, 2-7 are laid on the top of concrete flange. Considering the symmetry, the strain distributions of SLB1 and SLB2 at different load steps are shown in Figs. 9 and 10 respectively. Since the specimen was symmetrical and the loads were applied symmetrically, the strains in Figs. 9 and 10 were replicated symmetrically.

According to Figs. 9 and 10, the strains are approximately evenly distributed in the region of the compressive concrete in the whole loading process.

Strain gauges 3-6 and 2-4 are laid on the steel beam and concrete at the same height (Fig. 5), and the

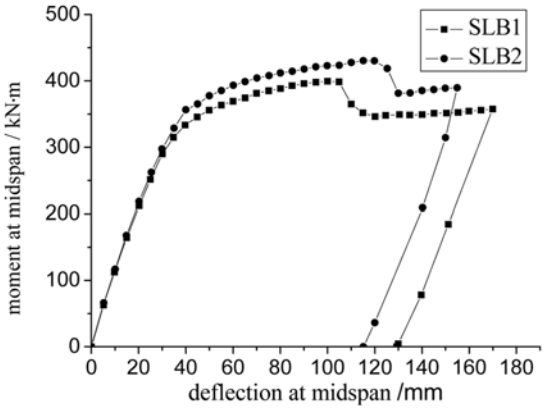

Fig. 8 Moment-deflection curves at midspan

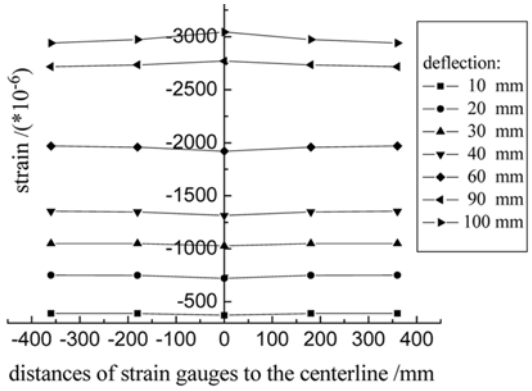

Fig. 9 Transverse distribution of strain in SLB1

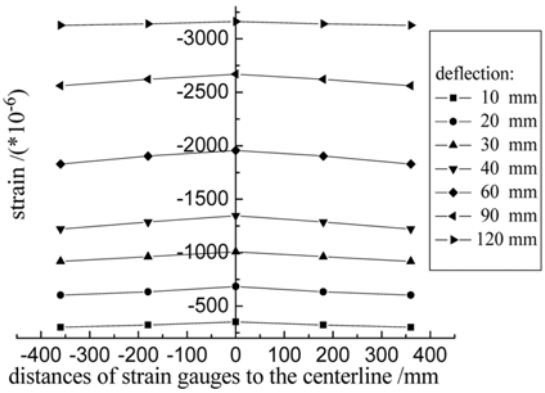

Fig. 10 Transverse distribution of strain in SLB2

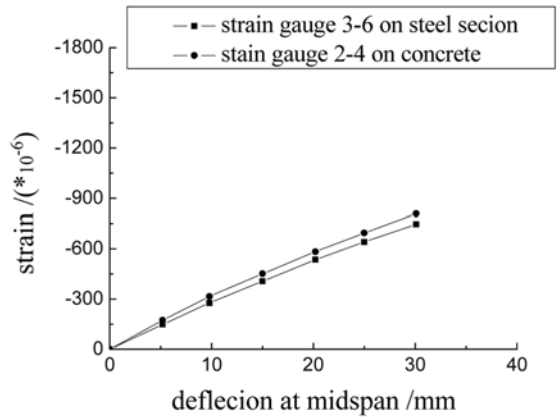

Fig. 11 Strain-deflection curves at midspan in SLB1

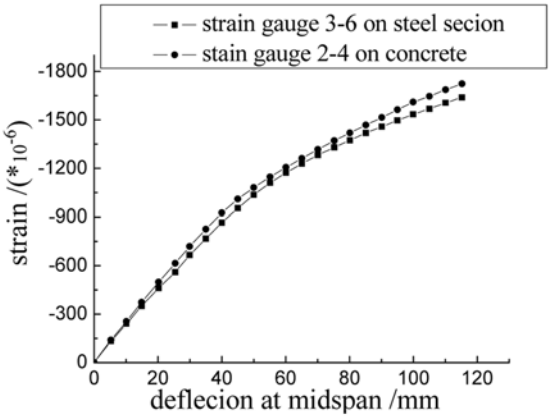

Fig. 12 Strain-deflection curves at midspan in SLB2

Note: Because the strain gauge 2-4 of SLB1 broke down during the loading process, only part of results are recorded

strain records of SLB1 and SLB2 are shown in Figs. 11 and 12 respectively. From the results, the strain of steel beam and concrete at the same height developed concurrently and are approximately equal not only in the elastic phase but also in elasto-plastic phase.

In addition, the results recorded by strain gauges 3-1, 3-2 which are on the bottom flange of steel section indicate that even distribution existed in the flanges of steel section within the elastic phase but not any more when turned into the elasto-plastic phase.

The above results shows that the transverse strain are approximately evenly distributed in the steel section and compression concrete which works together well within the elastic phase.

2.3.4 Vertical distribution of strain in the composite section

Figs. 13 and 14 show the results recorded by the six strain gauges on the vertical centerline of the composite section (see Fig. 5) at different load steps. According to the results, before the displacement

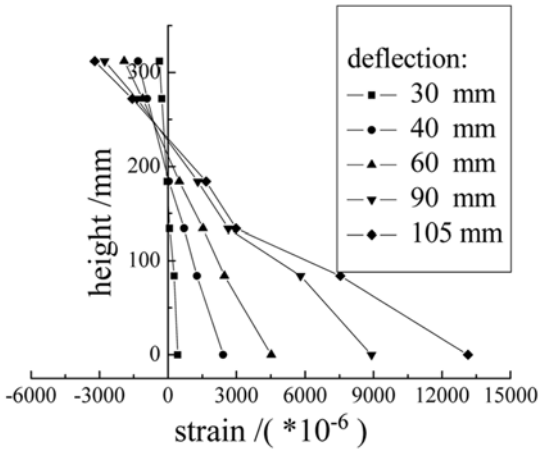

Fig. 13 Vertical distribution of strain in SLB1

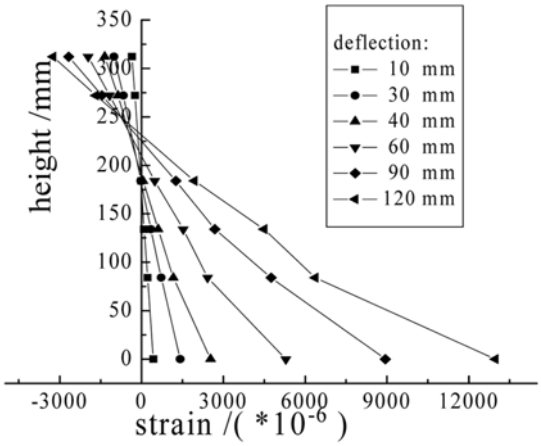

Fig. 14 Vertical distribution of strain in SLB2

of the specimen at midspan reached 1/200 of the length of the beam (30 mm), i.e. within the elastic phase, the vertical distribution of stains could be regarded as linear and the neutral axis was below the top of metal deck. Once turned into the elasto-plastic phase, the strain in the bottom flange of steel section increased fast, and the vertical distribution of strain was no more linear, meanwhile the neutral axis of the composite section moved upwards.

2.3.5 Strain distribution in concrete ribs

The strain gauges 2-1 and 2-2 recorded the strain values of the tension region in concrete ribs and the results were less than 50×10^{-6} during the loading process which indicated that the corresponding stress would be less than 1 MPa.

2.3.6 Test results

From the above test records, the following conclusions can be drawn:

(1) The separation on the interface in SLB2 imposes little influence on the loading capacity of the composite beam.
(2) Within the elastic stage, the steel and the concrete work together well and the composite section consists with Bernoulli's principle.
(3) The concrete rib in the deep deck flange shares little load during the loading process.

3. Flexural stiffness

3.1 Calculation section

Since the concrete ribs share little load, they can be neglected in the calculation section. Though the lower part of concrete will crack during the loading process, the calculation section will be assumed consistent with Bernoulli's principle for the major part of load will be resisted by the steel section in tensile region.

3.2 Stiffness coefficient in pure bending section

Before the deflection at midspan reaches 1/200 of the beam length, the deformation is supposed to be small and elastic, and the moment $M(x)$ can be given by:

$$M(x) = -EI(x)v''(x) \tag{1}$$

where $EI(x)$ and $v(x)$ are the stiffness and deflection of the beam section respectively, and the calculation diagram is illustrated in Fig. 15.

For a simply supported beam, if the load is specified, the section moment will be more or less dependent on the position of beam section. In Fig. 15, the section moment can be given by:

$$M_i(x) = \alpha(x) \cdot P_i \tag{2}$$

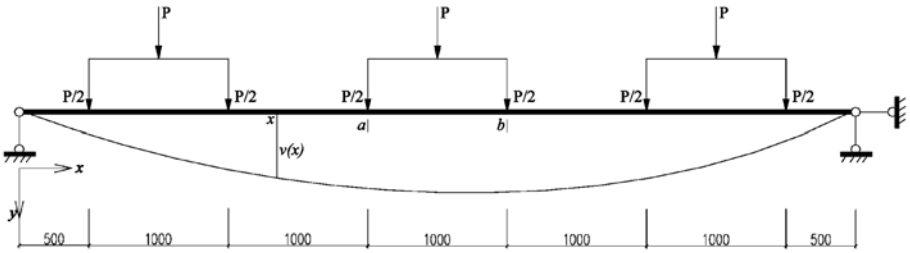

Fig. 15 Calculation diagram

where $\alpha(x)$ is the moment coefficient which is taken as 2.25 m for the pure bending region between section-a and section-b as obtained from the test; P_i is the applied load and i denotes the load step.

Therefore the flexural stiffness in pure bending section can be given by:

$$EI_i(x) = -\frac{\alpha \cdot P_i}{v_i''(x)} \tag{3}$$

Then, the stiffness coefficient in pure bending section is defined as:

$$\beta_i(x) = -\frac{P_i}{v_i''(x)} \tag{4}$$

Finally, Eq.(3) can be simplified as:

$$EI_i(x) = \alpha \cdot \beta_i(x) \tag{5}$$

3.3 Stiffness coefficient curves in pure bending section

The deformation of the beam is recorded by the displacement meters, and the deflection curves under different load steps are fitted by a polynomial (see Figs. 16 and 17).

According to the quintic polynomial, the curves of stiffness coefficient $\beta_i(x)$ in pure bending section

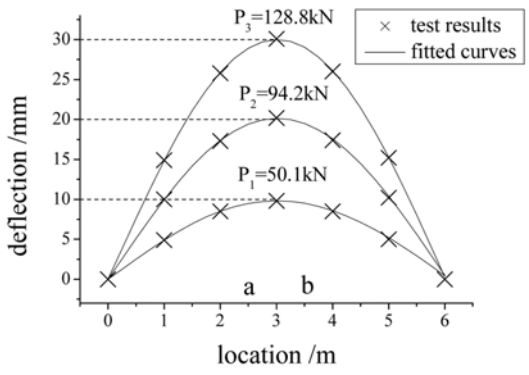

Fig. 16 Deflection curve of SLB1

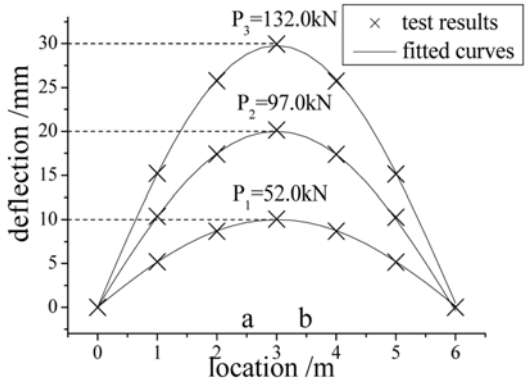

Fig. 17 Deflection curve of SLB2

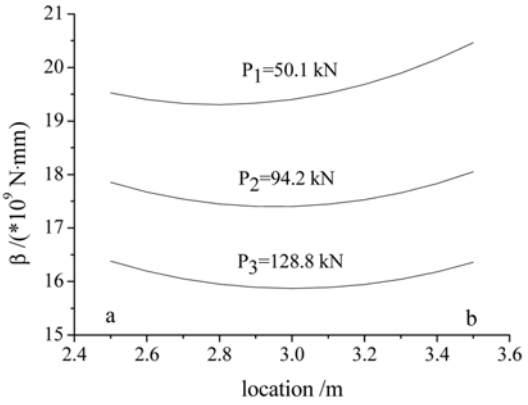

Fig. 18 Coefficient curve of flexural stiffness of SLB1

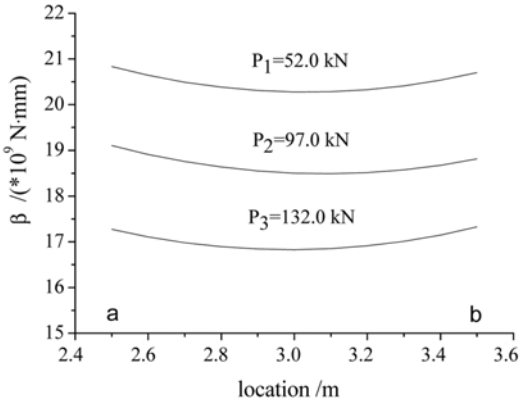

Fig. 19 Coefficient curve of flexural stiffness of SLB2

can be obtained from Eq.(4), as illustrated in Figs. 18 and 19.

The stiffness coefficient curves have following features:

(1) The curves are sagging but the differences between the maximum and minimum are less than 5%, therefore the flexural stiffness in pure bending section can be approximately regarded as equal.

(2) The stiffness coefficient will reduce with the load increasing, and the maximal decreasing amplitude will reach 17%. The concrete crack is the main reason for the stiffness reduction.

3.4 Average stiffness of coefficient curves in pure bending section

When calculating the deflection at midspan, the beam can be equivalent to one with a uniform flexural stiffness, and the average stiffness can be calculated based on the test deflection curves.

In Fig. 15, for a beam under six-point loading, the deflection at midspan can be given by:

$$v = \beta \cdot \frac{PL^3}{EI_e} \tag{6}$$

where L is the beam span and β is the stiffness coefficient at midspan which is 0.0395 for the simply supported beam under six-position loading.

Then the average flexural stiffness under different load steps can be given by:

$$EI_{ei} = \beta \cdot \frac{P_i \cdot L^3}{v_i} \tag{7}$$

where i denotes the load step.

From the test, the average flexural stiffnesses are listed in Tables 3 and 4. Meanwhile the stiffnesses at midspan which are obtained from Eqs.(4) and (5) are given for comparison.

From Tables 3 and 4, the differences between the average values and that at midspan are less than 3%.

3.5 Calculation method of flexural stiffness

Based on the comparison in section 3.4, the flexural stiffness at midspan is taken as the average

Table 3 Flexural stiffness of SLB1

Load P(kN)	Defleciton n v(mm)	Average stiffness EI_e(N*mm^2)	Stiffness at midspan EI(N*mm^2)	$(EI- EI_e)/EI$ (%)
50.1	9.8	4.36×10^{13}	4.37×10^{13}	0.23
94.2	20.2	3.98×10^{13}	3.92×10^{13}	−1.5
128.8	30.1	3.65×10^{13}	3.57×10^{13}	−2.2

Table 4 Flexural stiffness of SLB2

Load P(kN)	Defleciton n v(mm)	Average stiffness EI_e(N*mm^2)	Stiffness at midspan EI(N*mm^2)	$(EI- EI_e)/EI$ (%)
52.0	10.0	4.44×10^{13}	4.56×10^{13}	1.8
97.0	20.1	4.12×10^{13}	4.16×10^{13}	0.96
132.0	29.9	3.77×10^{13}	3.79×10^{13}	0.53

stiffness for simplification in this paper and the basic assumptions in the analysis of the flexural stiffness are shown as follows:

(1) Only the steel beam and the concrete above the deck top are considered, the concrete rib and rebar are neglected.

(2) The slippage between the concrete and steel beam is neglected and the composite section consists with Bernoulli's principle.

In the analysis, the equivalent section method is used. The parameters of the steel section and composite section are shown in Figs. 20 and 21 respectively.

where, B_e is the effective width of the composite beam;

D_s is the thickness of the concrete slab over the deep deck;

D_c is the thickness of the concrete slab over the steel beam;

D_d is the height of the deep deck;

y_{ec} denotes the position of elastic neutral axis (*e.n.a*) in composite section, which is given by:

$$y_{ec} = \frac{Ay_e + \frac{A_c}{\alpha_e}\left(\frac{D_s}{2} - D_c\right)}{A + \frac{A_c}{\alpha_e}} \tag{8}$$

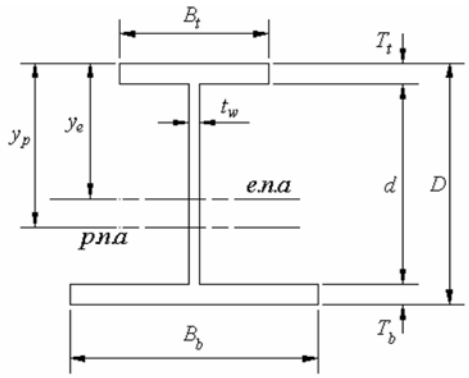

Fig. 20 Steel section

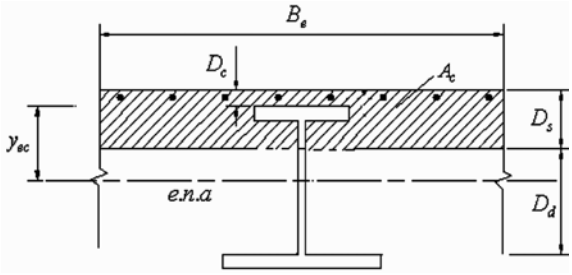

Fig. 21 Composite section for stiffness calculation

where A is the area of the steel section; $A_c = B_e D_s$ dnotes the area of the concrete section above the deck top; $\alpha_e = E_s / E_c$ denotes the elastic Young's modulus ratio of the steel to concrete material; y_e denotes the position of *e.n.a* in steel section (see Fig. 21).

Then, the elastic moment of inertia of the composite section can be obtained based Bernoulli's principle by:

$$I_c = I_x + A(y_e - y_{ec})^2 + \frac{A_c}{\alpha_e}\frac{D_s^2}{12} + \frac{A_c}{\alpha_e}\left(\frac{D_s}{2} - D_c - y_{ec}\right)^2 \tag{9}$$

where I_x denotes the elastic moment of inertia of the steel section.

Finally, the flexural stiffness of the composite section is $E_s I_c$.

The composite slim beam can serve as both the main beam and the secondary beam. According to Chinese standard *Code for design of steel structures (GB 50017-2003)*, the allowable deflections are L/400 and L/250 (L denotes the beam span) for the main beam and secondary beam respectively. The results obtained from Eqs.(8) and (9) are listed in Table 5 where the test values of average stiffness are also listed for comparison.

From Table 5, the calculation results are in good agreement with the results of main beam and slightly higher than those of the secondary beam.

4. Bending Resistance

4.1 Stress distribution in the ultimate limit state

The stress distributions on the vertical centerline of the composite section for both specimens in the

Table 5 Comparison of calculation and test results

	Calculation results		Test results	
	y_{ec} (mm)	E_sI_c (N/mm^2)	Average stiffness EI_e (N/mm^2) L/400*	L/250*
SLB1	97.2	4.10×10^{13}	4.16×10^{13}	3.81×10^{13}
SLB2	97.2	4.10×10^{13}	4.27×10^{13}	3.91×10^{13}

Note: L/400 and L/250 mean the test results when the deflection at midspan reached 1/400 and 1/250 of the beam span respectively.

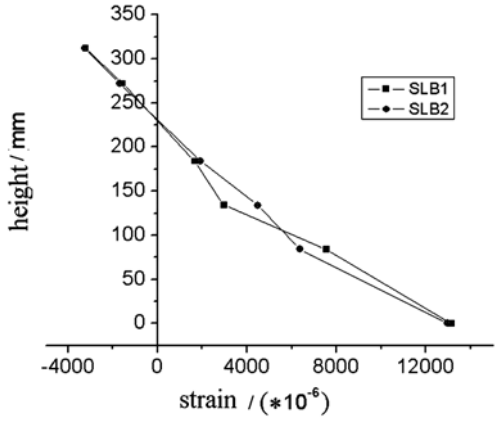

Fig. 22 Longitudinal strain distribution of sections in the ultimate limit state

ultimate limit state are shown in Fig. 22

From Figs. 13 and 14, the strain of concrete on the beam top has exceed the peak strain of the CL25 concrete which is 2470×10^{-6}, meanwhile, most of the steel section has entered into the state of plasticity. The stress distribution of the composite section can be deduced from the test results, as illustrated in Fig. 23.

4.2 Calculation method of bending capacity

4.2.1 Fundamental assumptions

The analysis of the bending capacity of the sagging moment region is based on the following assumptions:

(a) The steel beam and the rebar are all elastic-perfectly plastic body.
(b) The strain is uniformly distributed in the compression concrete which works together well with the steel beam, and the slippage between them is neglected.
(c) The concrete in the tensile region and concrete rib is neglected, so are the transverse reinforcing bars.
(d) The steel section is fully strain distribution at the ultimate limit state.

4.2.2 Equivalent stress distribution

At the ultimate limit state, the *p.n.a* is possibly located in the following three locations: (1) in the top

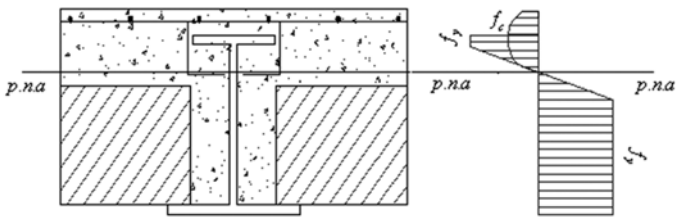

Fig. 23 Stress distribution of section at midspan

flange of the steel beam; (2) between the top flange and the deep deck; (3) in the deep deck. The three possible positions are illustrated in Fig. 24.

In state 2, the strain and stress distributions are shown in Fig. 25, where χ_c is the thickness of the concrete in compression, which is the distance from the neutral axis to the top surface; f_c is the peak stress of concrete; f_y is the yield stress of the steel beam; F_c is resultant force of the concrete in compression.

To simplify the calculation, the strain distribution is suggested as the equivalent rectangular stress distribution (Fig.25 (d)). The equivalence principles are given as following:

(a) The thickness of the concrete in compression is χ_c which is unchangeable.

(b) The resultant force of the concrete in compression is unchangeable and the peak stress is reduced by

$$f_{c,equ} = \gamma f_c \tag{10}$$

where γ is the reduction factor which will be introduced in detail later.

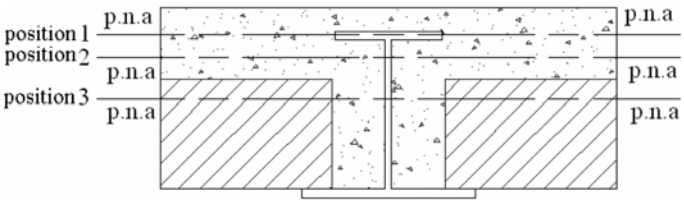

Fig. 24 The position of *p.n.a* in the sagging moment region

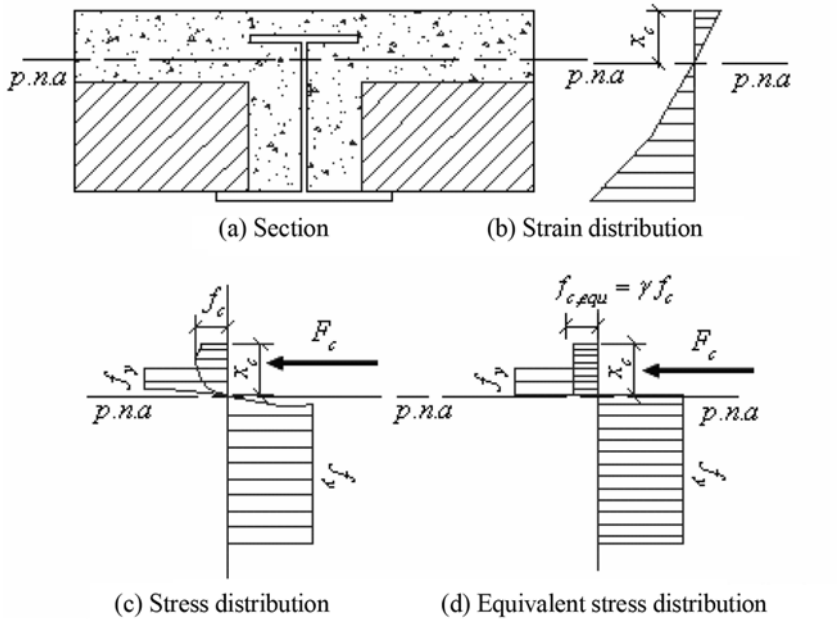

Fig. 25 Equivalent stress distribution when *p.n.a* in position 2

4.2.3 Calculation of bending capacity

The steel section is illustrated in Fig. 20 and the composite section for calculating the bending capacity is shown in Fig. 26 as follows.
where y_c denotes the position of plastic neutral axis (*p.n.a*) in composite section.

For position 2, according to Fig. 25, the distance from the natural axis to the top surface of the steel beam y_c and the bending capacity M_c can be given by:

$$y_c = \frac{2\frac{R_w}{d}y_p - \frac{R_c}{D_s}D_c}{2\frac{R_w}{d} + \frac{R_c}{D_s}} \tag{11}$$

and

$$M_c = M_s + \frac{R_c(y_p + D_c)(y_c + D_c)}{D_s \quad 2} \tag{12}$$

where, R_w is the tensile capacity of the web of steel section; M_s is the bending capacity of the steel section, R_c is the compression capacity of the concrete over the deck top, which is given by:

$$R_c = f_{c,equ}B_eD_s = \gamma f_cB_eD_s \tag{13}$$

For position 3, the equivalent stress distribution is illustrated in Fig. 27.
y_c and M_c can be given by:

$$y_c = y_p - \frac{R_c}{R_w}\frac{d}{2} \tag{14}$$

$$M_c = M_s + \frac{R_c(y_p + D_c)(y_c + D_c)}{D_s \quad 2} \tag{15}$$

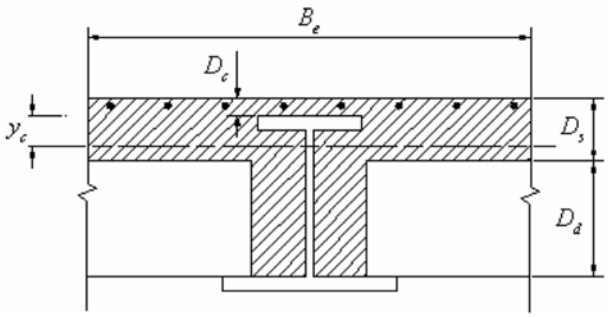

Fig. 26 Composite section for bending capactiy calculation

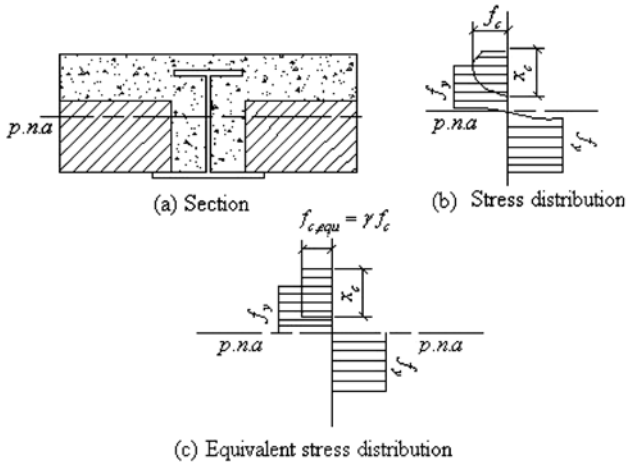

Fig. 27 Equivalent stress distribution when *p.n.a* in position 3

For state 1, since the thickness of the flange is very small, as a simplification, the *p.n.a* can be considered at the centerline of the top flange, that is

$$y_c = 0.5T_t \tag{16}$$

$$M_c = R_b\left(D - \frac{T_b + T_t}{2}\right) + \frac{R_w}{2}(d + T_t) + \frac{R_c}{D_s}\frac{D_c^2}{2} \tag{17}$$

where R_b is the tensile capacity of the bottom flange of the steel section.

4.2.4 Determination of the reduction factor γ

Since the measurement of accurate stress distribution in compression concrete is very difficult, in this paper the reduction factor γ is determined through an indirect method. In this method, the reduction factor is calculated from the position of *p.n.a* which is determined from the test results.

According to the test results, for both the specimens, the *p.n.a* are in position 2, therefore the reduction factor γ can be obtained from Eqs.(10) and (11), that is

$$\gamma = \frac{2\frac{R_w}{d}(y_p - y_c)}{f_c B_e (y_c + D_c)} \tag{18}$$

By substituting y_c which is obtained from the test result into Eq.(18), the reduction factors γ can be obtained, which are 0.542 and 0.559 for SLB1 and SLB2 respectively. In this paper, the reduction factor γ is suggested to be 0.55 which is lower than common reinforced concrete beam because the contribution of concrete part to ultimate bending capacity has been underestimated because of the classical plastic analysis. Then, the bending capacity of the specimens can be obtained from Eq.(12),

Table 6 Comparison of calculation and test results for SBL1 and SLB2

	y_p (mm)	y_c (mm)	γ	M_c (kN·m)	M_c^* (kN·m)	$\frac{M_c - M_c^*}{M_c^*}$
SLB1	213	41.8	0.55	422.3	399.3	5.8%
SLB2	213	41.8	0.55	422.3	430.5	-1.9%

Table 7 Comparison of calculation and test results for 280ASB and 300ASB

	y_p (mm)	y_c (mm)	γ	M_c (kN·m)	M_c^* (kN·m)	$\frac{M_c - M_c^*}{M_c^*}$
280ASB	200.8	110.8	0.55	729.1	789	-7.6%
300ASB	216.3	103.8	0.55	903.7	956	-5.5%

and the calculation results M_c are illustrated in Table 4, where the experimental results M_c^* are also illustrated for comparison.

From Table. 6, it can be seen that there is only little difference between M_c and M_c^*, and the proposed calculation method of bending capacity is validated by the test results.

In addition, the calculation method is also applied in the simply supported slim beams 280ASB and 300ASB which are conducted by R.M. Lawson, D.L. Mullett and etc (Lawson, *et al.* 1999). Since both the beams are in state 3, Eqs.(14) and (15) are used, and the results are illustrated in Table 7 for comparison.

From Table 7, the calculation results are conservative and in good agreement with the test results.

5. Conclusion

(1) During the loading process, the slippage on the interface is less than 0.2mm and the separation on the interface in SLB2 imposes little influence on the loading capacity of the composite beam.

(2) Within the elastic stage, the steel and the concrete work together well and the composite section consists with Bernoulli's principle. The concrete rib in the deep deck flange shares little load during the loading process

(3) Based on the test results, the flexural stiffness at midspan is suggested to be taken as the average stiffness for deflection calculation. A method of stiffness calculation is proposed based on Bernoulli's principle by which the calculation results are very close to test results when the deflection at midspan reached 1/300 of the beam span.

(4) At the ultimate limit state, the test results show that a plastic hinge can form at the midspan and the concrete ribs share little load. Based on the tests, a calculation method of bending capacity based on equivalent rectangular stress distribution is proposed. By this method, the common used composite slim beams can be classified as three states, and the bending capacity can be calculated separately.

(5) The reduction factor γ of equivalent stress distribution is determined as 0.55 which is verified by the test results. With the known quantity γ, the calculation of bending resistance will be feasible and convenient, and the results are conservative and in good agreement with the test results.

References

Bailey, C.G. (1999), "The behaviour of asymmetric slim floor steel beams in fire", *J. Constr. Steel Res*., **50**, 235-257.

Bailey, C.G. (2003), "Large scale fire test on a composite slim-floor system", *Steel Compos. Struct*., **3**(3), 153-168.

Bernuzzi, C., Gadotti, F. and Zandonini, R. (1995), "Semi-continuity in slim floor steel-concrete composite systems", *Proc. of the 1995 1st European Conf. on Steel Structures*, EUROSTEEL95, Athens, May.

Borgogno, W. and Fontana, M. (1998), "Fire safety of slim floor composite slabs with precast prestressed hollow core elements", *Stahlbau*, **67**(10), 776-784.

Borgogno, W. and Fontana, M. (2000), "Structural behaviour of slim floor slabs with prestressed hollow core elements at room temperature and in fire", *Proc. of the Conf.: Composite Construction in Steel and Concrete IV*, Banff, May-Jun, 768-779.

Chen, Q., Shi, Y.J., Wang, Y.Q., Chen, H. and Zhang, Y. (2002), "Structural analysis on light steel frame with steel-concrete composite slim beam", *Building Structures*, **32**(2), 17-20.

Hicks, S., Lawson, R.M. and Lam, D. (2006), "Design considerations for composite beams using precast concrete slabs", *Composite Construction in Steel and Concrete V - Proc. of the 5th Int. Conf*., Mpumalanga, Jul, 190-201.

Hicks, S.J. and Lawson, R.M. (2003), *Design of composite beams using precast concrete slabs*, SCI Publication 287, The Steel Construction Institute, Ascot.

Lange, J. (2006), "Design of edge beams in slim floors using precast hollow core slabs", *Composite Construction in Steel and Concrete V - Proc. of the 5th Int. Conf*., Mpumalanga, Jul, 260-269.

Lawson, R.M., Bode, H., Brekelmans, J.W.P.M., Wright, P.J. and Mullet, D.L. (1999), "Slimflor and slimdek construction: European developments", *Struct. Eng*., **77**(8), 28-32.

Lawson, R.M., Mullett, D.L. and Rackham, J.W. (1998), "Design of Asymmetric Slimflor Beams", *Proc. of the 1998 2nd World Conf. on Steel in Construction*, San Sebastian, May.

Lu, X.H. and Makelainen, P. (1995), "Strength and Stiffness of Composite Slim Floor Beams", *Proc. of the 4st Pacific Structural Steel Conf*., Singapore 95, Singapore, 93-100.

Lu, X.H. and Makelainen, P. (1995), "Parametric Studies on Steel-concrete Composite Beams in Slim Floors", *Proc. of the 1st European Conf. on Steel Structures*, EUROSTEEL95, Athens, May, pp.18-20.

Lu, X.T. and Zhang, S.M. (2005), "Analysis of the temperature distribution in composite slim floor beams subjected to fires", *Journal of Harbin Institute of Technology*, **37**(2), 446-450.

Lu, X.T. and Zhang, S.M. (2005), "Numerical analysis of composite slim floor beams in fire", *Journal of Harbin Institute of Technology*, **37**(2), 442-445.

Ma, Z.C. and Makelainen, P. (2006), "Structural behaviour of composite slim floor frames in fire conditions", *J. Constr. Steel Res*., **62**, 12821289.

Makelainen, P. and Ma, Z.C. (2000), "Fire resistance of composite slim floor beams", *J. Constr. Steel Res*., **54**, 345-363.

Malaska, M. (2000), "Behavior of a Semi-continuous Beam-column Connection for Composite Slim floors", PhD Thesis, Helsinki University of Technology, Helsinki, Finland.

Queiroz, G. and De Paula, F.A. (2000), "Calibration of a FE model for the analysis of slim composite floors", *Proc. - Annual Technical Session*, Structural Stability Research Council, Memphis, Jul, 288-300.

Sha, W. (2001), "Fire resistance of protected asymmetric slim floor beams", *Proc. of the Eighth Int. Conf. on Civil and Structural Engineering Computing*, Vienna, Austria, Sept., 167-168

Sha, W. (2001), "Fire resistance of slim floors protected using intumescent coatings", *Proc. of the Eighth Int. Conf. on Civil and Structural Engineering Computing*, Vienna, Austria, Sept., 163-164.

Yang, L., Shi, Y.J., Wang, Y.Q., *et al*. (2006), "Analysis of effective width of simply supported composite slim floor", *9th Int. Symposium on Structural Engineering for Young Experts*, Fuzhou, Aug, 398-403.

Zandonini, R., Gadotti, F. and Fedrizzi, E. (2003), "Composite steel-concrete systems with slim floor beams: structural performance and design considerations", *Advances in Structures*, ASSCCA 03, Sydney, Jun, **1-2**, 35-44.